

Combating fluctuations in relaxation times of fixed-frequency transmon qubits with microwave-dressed states

Peng Zhao,^{1,*} Teng Ma,^{1,†} Yirong Jin,^{1,‡} and Haifeng Yu¹

¹*Beijing Academy of Quantum Information Sciences, Beijing 100193, China*

(Dated: June 9, 2022)

With the long coherence time, the fixed-frequency transmon qubit is a promising qubit modality for quantum computing. Currently, diverse qubit architectures that utilize fixed-frequency transmon qubits have been demonstrated with high-fidelity gate performance. Nevertheless, the relaxation times of transmon qubits can have large temporal fluctuations, causing instabilities in gate performance. The fluctuations are often believed to be caused by nearly on-resonance couplings with sparse two-level-system (TLS) defects. To mitigate their impact on qubit coherence and gate performance, one direct approach is to tune the qubits away from these TLSs. In this work, to combat the potential TLS-induced performance fluctuations in a tunable-bus architecture unitizing fixed-frequency transmon qubits, we explore the possibility of using an off-resonance microwave drive to effectively tuning the qubit frequency through the ac-Stark shift while implementing universal gate operations on the microwave-dressed qubit. We show that the qubit frequency can be tuned up to 20 MHz through the ac-Stark shift while keeping minimal impacts on the qubit control. Besides passive approaches that aim to remove these TLSs through more careful treatments of device fabrications, this work may offer an active approach towards mitigating the TLS-induced performance fluctuations in fixed-frequency transmon qubit devices.

I. INTRODUCTION

With the advantages of long coherence times [1–4] and simplified demands on the electronic control circuits, fixed-frequency transmon qubit [5] has been demonstrated as a leading qubit modality for quantum computing [1]. This can be partially manifested by the progress that diverse qubit architectures, which utilize fixed-frequency transmon qubits, have been demonstrated with high-fidelity gate performance, such as all-microwave controlled qubit architecture with fixed inter-qubit coupling [6–13], qubit architecture with tunable bus [14] or tunable coupler [15, 16], and qubit architecture combining both fixed-frequency qubits and frequency-tunable qubits [17]. However, just the same as frequency-tunable transmon qubits [18], the relaxation times of fixed-frequency transmon qubits can show large temporal fluctuations [19–21]. Since the current gate performance approaches the qubit coherence limit [1], the fluctuations can lead to prominent performance instabilities in transmon qubit devices [17, 22].

For transmon qubit devices, the fluctuations in relaxation times are often believed to be attributed to nearly on-resonance couplings with sparse two-level-system (TLS) defects [18–21]. The TLS defect can act as environmental noise coupled to the qubit with the noise spectral density peaked around its frequency. As the frequency of the TLS defect can have temporal fluctuations due to its couplings to thermally fluctuating defects (i.e., low-frequency TLSs with frequencies less than $k_B T$, where k_B is the Boltzmann constant and T is the working temperature of the qubit devices, typically, 10 mK), this could explain the fluctuations in relaxation times of transmon qubits [23–26]. Meanwhile, in conditions where qubit relaxations contain non-negligible contributions

from quasiparticles, the variations of qubit relaxation times could also be attributed to the fluctuation in the quasiparticle density near the qubit junctions [27–29] or the fluctuations in quasiparticle dissipation channels [30, 31]. Nevertheless, for well-shielded transmon qubit devices, transmon qubits have been shown not yet limited by losses related to quasiparticles [4]. Additionally, a recent result also suggests that quasiparticles trapped in shallow subgap states can also behave similarly to TLS [32].

Generally, the existence of performance fluctuations suggests that, to maintain a reliable and high-fidelity gate performance, rapid and frequent qubit characterizations are needed [33]. Moreover, besides being frequently re-characterized for detecting and tracking these fluctuations, one has also to actively mitigate the detrimental impact on gate performance. For the state-of-the-art transmon qubit devices, the TLS defects that are coupled strongly or nearly on-resonantly to qubits are generally sparse [18, 21]. Thus, to mitigate the TLS-induced performance fluctuations, the direct and active approach is to tune the qubit away from the dominant TLS defect, and then a re-calibration of gate operations should be employed to find new optimal control parameters [33]. We note that ultimately, passive approaches that aim to remove the detrimental TLS defects through more advanced fabrication technology, should work successfully, but currently, the exact nature of the TLS defect is still unknown [34] and this active approach may be a more practical solution.

For fixed-frequency transmon qubits, to mitigate TLS-induced performance fluctuations, one can effectively tune its frequency through the off-resonance drive induced ac-Stark shift [21, 35–37], and choose the microwave-dressed qubit states as the basis states of a new qubit, i.e., the dressed qubit [13, 38–42]. In this way, gate operations should be implemented on this microwave-dressed basis. However, while the ac-Stark shift has been recognized as an effective tool for tuning qubit frequency, its compatibility with the gate operations on superconducting qubits is less studied [13, 40, 42]. In this work, to combat the potential TLS-induced perfor-

*Electronic address: shangniguo@sina.com

†Electronic address: mateng@baqis.ac.cn

‡Electronic address: jinyr@baqis.ac.cn

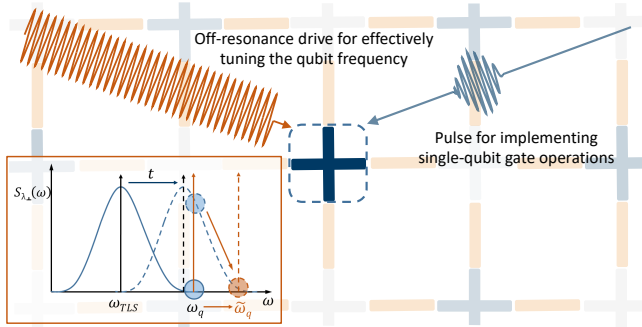


FIG. 1: Illustration of mitigating TLS-induced relaxation fluctuations of a qubit through the off-resonance drive induced ac-Stark shift. The inset shows how the fluctuation in qubit relaxation times occurs due to its coupling to a dominant TLS for which its frequency can have temporal fluctuation, and how to mitigate the relaxation fluctuations through tuning the qubit away from the TLS, i.e., tuning from ω_q (solid orange (light gray) arrow) to $\tilde{\omega}_q$ (dashed orange (light gray) arrow). Blue solid curve denotes the noise spectral density peaked at the TLS's frequency ω_{TLS} (solid black arrow), blue dashed line for the case when fluctuations in the TLS's frequency occurs (dashed black arrow) due to its couplings to thermally fluctuating defects (low-frequency TLS defects).

mance fluctuations in a tunable-bus architecture unitizing fixed-frequency transmon qubits [43], we examine the possibility of tuning the qubit away from the dominant TLS defect through the ac-Stark shift while implementing universal qubit control, including gate operations, qubit initialization, and readout, on the microwave-dressed qubit. We show that although parasitic interactions induced by the stark drive exist, one can still mitigate their detrimental impacts on qubit control. Thus, using the stark drive, the qubit frequency can be tuned up to 20 MHz while keeping minimal impacts on the qubit control.

The rest of the paper is organized as follows. In Sec. II, we give brief descriptions of the microwave-dressed qubit, showing how to mitigate the detrimental effect from a dominated TLS defect through the ac-Stark shift. In Sec. III, in a tunable-bus architecture, we examine the possibility of implementing universal qubit control, including gate operations, qubit initialization, and readout, for the microwave-dressed qubit. In Sec. IV, we give discussions on the feasibility of the proposed scheme for mitigating TLS-induced performance fluctuations. Finally, we give conclusions of our investigation in Sec. V.

II. COMBATING TLS-INDUCED FLUCTUATIONS WITH MICROWAVE-DRESSED STATES

Here, firstly, for easy reference and to set the notation, we briefly review some basic properties of the qubit subjected to an off-resonance stark drive, including the ac-Stark shift and the decoherence of the qubit in the presence of the stark drive. Accordingly, in the following discussion, we call the qubit subjected to a stark drive as microwave-dressed qubit or dressed qubit, and call the undriven qubit as the bare qubit.

Then, we illustrate the mechanism of mitigating the detrimental effect from a dominated TLS defect through the ac-Stark shift.

A. ac-Stark shift

Here, as shown in Fig. 1, we consider a transmon qubit driven by an always-on off-resonance microwave drive. For illustration purposes only, the qubit is treated as an ideal two-level system. Thus, the Hamiltonian of this driven qubit system can be written as $H = \omega_q \sigma_z/2 + \Omega_s \cos(\omega_s t) \sigma_x$ (hereinafter, we set $\hbar = 1$), where ω_q denotes the bare qubit frequency, ω_s and Ω_s represent the frequency and the amplitude of the drive (hereafter called stark drive) which is introduced to induce an ac-Stark shift for the qubit. After applying the rotating wave approximation (RWA), and moving into the rotating frame with respect to the stark drive, the Hamiltonian becomes $H_r = \Delta_s \sigma_z/2 + \Omega_s \sigma_x/2$, where $\Delta_s = \omega_q - \omega_s$ denotes the detuning of the qubit from the stark drive frequency. Finally, considering the unitary transformation $U_1 = \exp(-i\theta \sigma_y/2)$ with $\theta = \arctan(\Omega_s/\Delta_s)$, H_r can be diagonalized and expressed as $H_{\text{eff}} = \Delta Z/2$ with $\Delta = \sqrt{\Delta_s^2 + \Omega_s^2}$. Here, $Z \equiv \cos \theta \sigma_z + \sin \theta \sigma_x$ denotes the Pauli operator defined in the dressed basis (i.e., the eigenstates of H_r)

$$\begin{aligned} |1\rangle &\equiv \sin \frac{\theta}{2} |g\rangle + \cos \frac{\theta}{2} |e\rangle, \\ |0\rangle &\equiv \cos \frac{\theta}{2} |g\rangle - \sin \frac{\theta}{2} |e\rangle, \end{aligned} \quad (1)$$

According to the above discussion, for the microwave-driven qubit, the ac-Stark shift can be expressed as $\delta\omega = \Delta - \Delta_s \approx \Omega_s^2/(2\Delta_s)$. However, since the transmon qubit is naturally a multilevel system with a weak anharmonicity [5], its higher energy levels can give non-negligible contributions on the stark shift $\delta\omega$. Thus, modeling the transmon qubit as an anharmonic oscillator with the anharmonicity η and taking the higher energy levels, especially the second excited state $|f\rangle$, into considerations, the Ac-stark shift [21, 36] can be approximated as (the second-order perturbation result)

$$\delta\omega \approx \frac{\Omega_s^2}{2\Delta_s} - \frac{(\sqrt{2}\Omega_s)^2}{4(\Delta_s + \eta)} = \frac{\eta\Omega_s^2}{2\Delta_s(\Delta_s + \eta)}. \quad (2)$$

B. Decoherence of the microwave-dressed qubit

We now discuss the environment-induced decoherence of the microwave-dressed qubit. The environment noise coupled to the qubit can be described as $H_{\delta\lambda} = \delta\lambda_z \sigma_z/2 + \delta\lambda_{\perp} \sigma_{\perp}/2$, where σ_{\perp} represents the transverse Pauli component, $\delta\lambda_z$ and $\delta\lambda_{\perp}$ denote the fluctuations in qubit parameters caused by the environment noise transversally and longitudinally coupled to the qubit, respectively.

Here, we consider that $S_{\lambda}(\omega) \equiv 1/(2\pi) \int dt \langle \delta\lambda(0) \delta\lambda(t) \rangle e^{-i\omega t}$ denotes the quantum noise spectral density associated with parameter λ . Taking into

account that the transmon qubit devices generally work at very low temperatures ($\omega_q \gg k_B T$), we neglect the absorption process involving $S_{\lambda\perp}(-\omega)$, and only consider the emission process involving $S_{\lambda\perp}(+\omega)$ (here, $\omega \simeq \omega_q$) [44]. Thus, the relaxation time \tilde{T}_1 and the pure dephasing time \tilde{T}_ϕ of the microwave-dressed qubit can be expressed as [44, 45]

$$\begin{aligned}\frac{1}{\tilde{T}_1} &= \pi \left[\frac{1 + \cos^2 \theta}{4} \frac{\tilde{S}_{\lambda\perp}(\omega_s, \Delta)}{2} + \sin^2 \theta S_{\lambda z}(\Delta) \right], \\ \frac{1}{\tilde{T}_\phi} &= \pi \left[\cos^2 \theta S_{\lambda z}(0) + \frac{\sin^2 \theta}{4} S_{\lambda\perp}(\omega_s) \right],\end{aligned}\quad (3)$$

with $\tilde{S}_{\lambda\perp}(\omega_s, \Delta) = S_{\lambda\perp}(\omega_s + \Delta) + S_{\lambda\perp}(\omega_s - \Delta)$. The above equation shows that due to the stark drive induced state hybridization, the environmental noise, transversally (longitudinally) coupled to the bare qubit, can contribute to the dephasing (relaxation) of the microwave-dressed qubit. Moreover, for the qubit relaxation, both the transverse noises at the sideband frequencies $\omega_s + \Delta$ and $\omega_s - \Delta$ contribute to the relaxation (depolarization) of the dressed qubit. This notable feature can be captured by a qualitative picture, i.e., depending on the parameters (e.g., detuning and magnitude) of external drives (stark drives), the drives could act as distinct noise spectral filters, allowing the qubits, i.e., spectrometers, to sense the environment noise differently in frequency space [45, 46].

C. Mitigating TLS-induced coherence degradation

For the state-of-the-art transmon qubit devices, the TLS defects that are coupled strongly or nearly on-resonantly to qubits are generally sparse [18, 21]. Therefore, one may reasonably expect that when prominent degradations in qubit relaxation times occur, the dominated contribution could be attributed to a single TLS defect that is coupled nearly on-resonantly to the qubit [18, 20, 21]. As shown in the inset of Fig. 1, as the dominated TLS defect can generally act as an environmental noise with the spectral density $S_{\lambda\perp}(\omega)$ peaked around its frequency ω_{TLS} , pushing the qubit frequency away from ω_{TLS} , i.e., from ω_q to $\tilde{\omega}_q$, can mitigate its impact on the qubit relaxation time. This mitigation procedure can be further explained by Eq. (3), which gives the expression of the relaxation rate $1/\tilde{T}_1$. Specifically speaking, for the TLS-induced noise peaked at ω_{TLS} , by carefully choosing the stark drive frequency ω_s and the drive amplitude Ω_s , only the noise at $\omega_s \pm \Delta$, in which the amplitude of the noise spectral density is far less than that at ω_{TLS} , contributes to the qubit relaxation. Thus, the ac-Stark shift can be introduced to protect the qubit from the TLS noise peaked at its frequency.

Note that compared with the bare qubit, there are two additional decoherence channels for the microwave-dressed qubit: (i) the amplitude-fluctuations, phase-fluctuations, and frequency-fluctuations of the stark drive can also act as an additional channel contributing to qubit dephasing or relaxation [13, 47–49]; (ii) For the case of a two-level qubit, the computational basis, i.e., Eq. (1), only involves the $\{|g\rangle, |e\rangle\}$. However, since the transmon qubit is a multilevel system, the

higher energy levels of the transmon qubit, such as $|f\rangle$, are also involved in the definition of the computational basis for the dressed transmon qubit. This could give rise to an additional dephasing or relaxation channel [12, 53].

III. QUBIT CONTROL WITH DRESSED-BASIS IN TUNABLE-BUS ARCHITECTURES

In this section, we examine the possibility of implementing universal control on the microwave-dressed transmon qubit, including gate operations, state initialization, and readout for the dressed qubit. In the following discussion, we give our analysis on a tunable-bus architecture, where two fixed-frequency transmon qubits Q_1 and Q_2 are coupled via a tunable bus Q_t [43]. In this tunable-bus architecture, the bus can mediate an effective ZZ coupling between the two qubits. One can turn off the ZZ coupling when implementing single-qubit control, such as single-qubit gate operations, state initialization, and readout. When turning on the ZZ coupling, two-qubit controlled-Z (CZ) gates can be realized.

In the presence of a stark drive applied to one of the two fixed-frequency qubits, the system Hamiltonian can be expressed as (here for illustration purpose only, the stark drive is applied to Q_1)

$$\begin{aligned}H = & \sum_{i=1,2,t} \left[\omega_i a_i^\dagger a_i + \frac{\eta_i}{2} a_i^\dagger a_i^\dagger a_i a_i \right] \\ & + \sum_{k=1,2} \left[g_k (a_t^\dagger a_k + a_t a_k^\dagger) \right] \\ & + \frac{\Omega_s}{2} (a_1^\dagger e^{-i\omega_s t} + a_1 e^{+i\omega_s t}),\end{aligned}\quad (4)$$

where the subscript $i = \{1, 2, t\}$ labels Q_i with anharmonicity η_i and bare mode frequency ω_i , a_i (a_i^\dagger) is the annihilation (creation) operator for Q_i , and g_k denotes the coupling strength between the tunable bus Q_t and the qubit Q_k . As in Sec. II A, in the presence of the stark drive applied to Q_1 , we can define the microwave-dressed qubit states of Q_1 as the basis states for qubit control. In this way, the tunable bus can mediate an effective ZZ coupling between the bare qubit Q_2 and the microwave-dressed qubit Q_1 [43].

Similar to the procedure given in Sec. II A, after applying the RWA and moving into the rotating frame with respect to the stark drive, the ZZ coupling strength, which is defined as $\zeta_{ZZ} \equiv (E_{11} - E_{10}) - (E_{01} - E_{00})$, can be obtained by diagonalizing the system Hamiltonian. Here, E_{jk} denotes eigenenergy of microwave-dressed qubit system associated with doubly dressed eigenstate $|j\tilde{k}\rangle$ (involving both state hybridizations from the stark drive and the qubit-bus coupling), which is adiabatically connected to the bare state $|j0k\rangle$ (hereafter, notation $|Q_1 Q_t Q_2\rangle$ is used, denoting the system state). Figures 2(a-c) show the strength of the ZZ coupling between Q_2 and dressed Q_1 as a function of the bus frequency ω_t and the detuning Δ_s (here denoting the detuning of Q_1 from the stark drive). The used system parameters are: qubit frequency $\omega_{1(2)}/2\pi = 5.0(5.2)$ GHz, anharmonicity $\eta_1 = \eta_2 = \eta_t = \eta$ with $\eta/2\pi = -300$ MHz, and qubit-bus

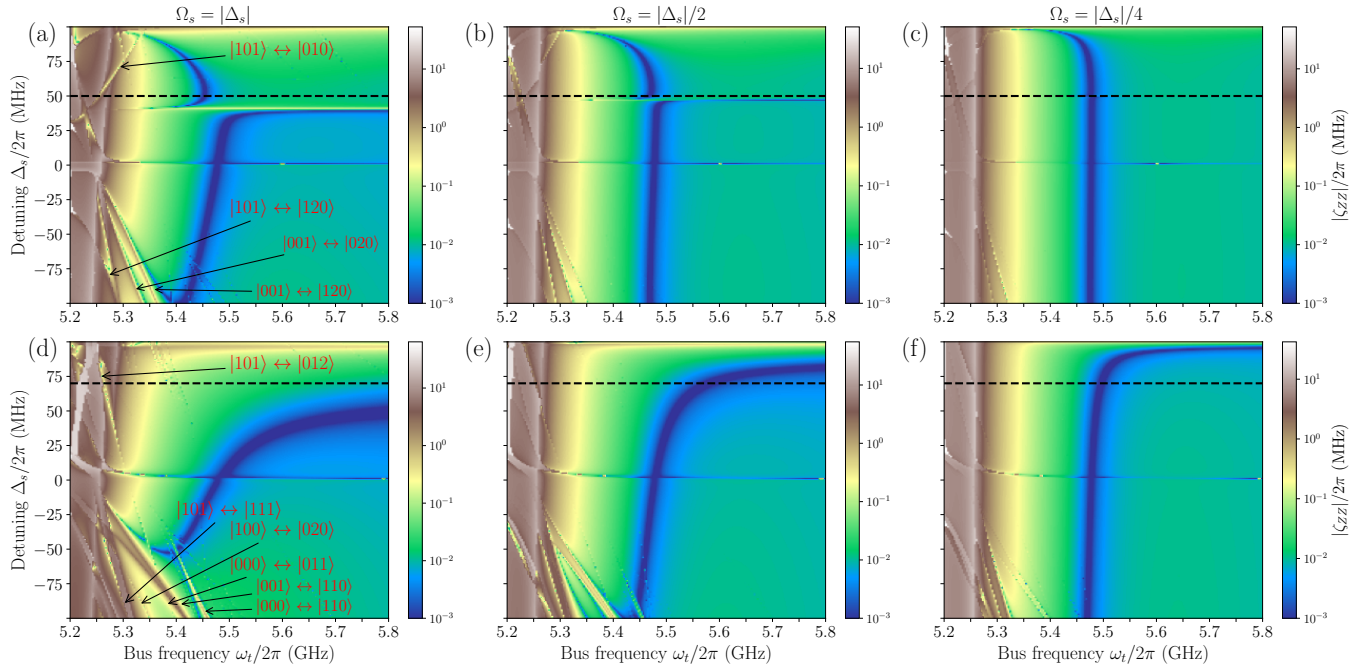


FIG. 2: ZZ coupling strength ζ_{ZZ} as a function of the bus frequency (ω_t) and the detuning (Δ_s) of qubit from the applied stark drive frequency. Here, the system parameters are: qubit frequency $\omega_{1(2)}/2\pi = 5.0(5.2)$ GHz, anharmonicity $\eta_1 = \eta_2 = \eta_t = \eta$ ($\eta/2\pi = -300$ MHz), and qubit-bus coupling $g_{1(2)} = g$ ($g/2\pi = 25$ MHz) (at $\omega_{1(2)} = \omega_t = 5.5$ GHz). (a-c) The stark drive is applied to Q_1 , and (d-f) for Q_2 . The amplitude Ω_s of the stark drive are $|\Delta_s|$ in (a,d), $|\Delta_s|/2$ in (b,e), and $|\Delta_s|/4$ in (c,f). The black arrows indicate the dips and peaks due to the presence of the stark drive induced parasitic interactions (red (light gray) texts). These interactions involve multi-excitation transitions, which are enabled by high-order processes, as indicated by the states involved in the transitions. Thus, the strengths are generally far smaller than that of the qubit-bus couplings and the drive. Moreover, the stark drive also act as the leading contribution. This can explain that by decreasing the drive amplitude Ω_s , the dips and peaks slowly disappear. The horizontal black dashed lines indicate examples of the stark drive frequencies (Δ_s) for Q_1 and Q_2 that are chosen to avoid the detrimental parasitic interactions caused by the applied stark drives.

coupling $g_{1(2)} = g\sqrt{\omega_{1(2)}\omega_t/\omega_{\text{ref}}^2}$ with $g/2\pi = 25$ MHz and $\omega_{\text{ref}}/2\pi = 5.5$ GHz [50]. In Figs. 2(a), 2(b), and 2(c), the stark drive amplitudes Ω_s are $|\Delta_s|$, $|\Delta_s|/2$, and $|\Delta_s|/4$, respectively. In Figs. 2(d-f), we also show the results for the stark drive applied to Q_2 , showing the ZZ coupling between the bare qubit Q_1 and the microwave-dressed qubit Q_2 .

As shown in Figs. 2, compared with the result in Ref.[43], the presence of the stark drive causes two prominent features:

(i) Both the zero- ZZ point and the interaction point for resonance coupling between $|101\rangle$ and $|020\rangle$, which are used for implementing CZ gates [43], are shifted. In addition, in some scenarios, the zero- ZZ point can disappear. This is to be expected, as the off-resonance stark drive can contribute an additional ZZ coupling due to different ac-Stark shifts of the computational states [12, 13, 51-54].

(ii) There are several dips and peaks in the ZZ coupling. After examining the system spectrum, we find that these dips and peaks result from the resonance interactions involving the qubits and the bus, as marked in Fig. 2. Moreover, the stark drive induced transitions also participate in the processes that enable these resonance interactions. This can explain that by decreasing the drive amplitude Ω_s , e.g., from Fig. 2(a) to Fig. 2(c), these dips and peaks slowly disappear. Since these

interactions are enabled by high-order processes, the coupling strengths are generally far smaller than that of the qubit-bus couplings and the off-resonance drive, and the energy gaps of their associated anti-crossings typically range from sub-MHz to a few MHz. Similar to the result discussed in Ref.[43], for implementing fast diabatic CZ gates [55], the presence of these parasitic interactions will give rise to a trade-off between the error resulting from the desired interaction involving $|101\rangle$ and $|020\rangle$ and the error from these parasitic resonance interactions with tiny energy gaps. Generally speaking, during the CZ gate operations, a slow gate-speed is better for mitigating the leakage from $|101\rangle$ to $|020\rangle$ (or leakage involving other interactions with larger coupling strengths, such as the bus-qubit interactions, which can potentially cause the leakage from the qubits to the bus). However, to mitigate the leakage error from these parasitic interactions with tiny anti-crossings, short-time gates are better.

According to the above discussion, to ensure high-fidelity two-qubit gate operations, the stark drive frequency (i.e., detuning Δ_s) should be chosen carefully to avoid inducing parasitic interactions. Without a doubt, this will limit the available range of the frequency and the amplitude of the stark drive. However, as shown in Fig. 2, there still exists available parameter regions, for which one can avoid the detriment-

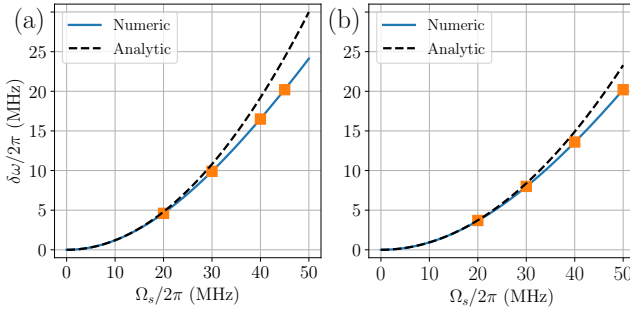


FIG. 3: The ac-stark shift versus the magnitude of the stark drive. (a) The detuning of the stark drive applied to Q_1 is $\Delta_s/2\pi = 50$ MHz, as marked in Figs. 2(a-c). (b) The detuning of the stark drive applied to Q_2 is $\Delta_s/2\pi = 70$ MHz, as marked in Figs. 2(d-f). Other system parameters are the same as those used in Figs. 2. The blue (light gray) solid lines denote the results obtained by numerical calculation, and the black dashed lines for analytical method, i.e., according to Eq. (2). The orange squares mark the stark drive amplitudes which are used in Sec. III B.

tal parasitic interactions. As an example, the black dashed lines in Figs. 2(a) and Figs. 2(d) denote suitable frequencies ($\Delta_s/2\pi = \{50, 70\}$ MHz) of the stark drives applied to Q_1 and Q_2 , respectively. Accordingly, Figures 3(a) and 3(a) show the ac-stark shift $\delta\omega$ versus the stark drive amplitude Ω_s . The results shown in Fig 2 and Fig 3 indicate that by varying the amplitude of the applied stark drive from 0 to 50 MHz, the ac-stark shift of the dressed qubit can be continually tuned from 0 to 20 MHz while avoiding detrimental parasitic interactions induced by the stark drives themselves.

In the following discussion, for illustration purposes, to examine the performance of qubit control on the dressed qubits, the detuning Δ_s are chosen as 50 MHz and 70 MHz for the stark drives applied to the Q_1 and Q_2 , respectively. Additionally, we restrict our discussion to the case where the stark drive is only applied to one of the two qubits. The main reason will be given in Sec. IV.

A. Qubit initialization and readout

In the presence of the always-on stark drive, the computational basis is the microwave-dressed basis. Therefore, the qubit control, including qubit initialization and readout, should be also operated on the dressed state. Similar to the procedure designed for dressed spin qubits [56] or Floquet qubits [57], by slowly ramping up or down the amplitude of the stark drive, the bare qubit states $\{|g\rangle, |e\rangle\}$ and the dressed qubit states $\{|0\rangle, |1\rangle\}$ can be adiabatically mapped to each other, thus enabling the initialization and readout of the dressed qubit. In this way, the qubit initialization can be realized by firstly initializing the qubit in the bare qubit state, e.g. $|g\rangle$, and then adiabatically mapping to the corresponding dressed state, e.g. $|0\rangle$. While for implementing qubit readout, the reverse procedure is firstly applied, thus

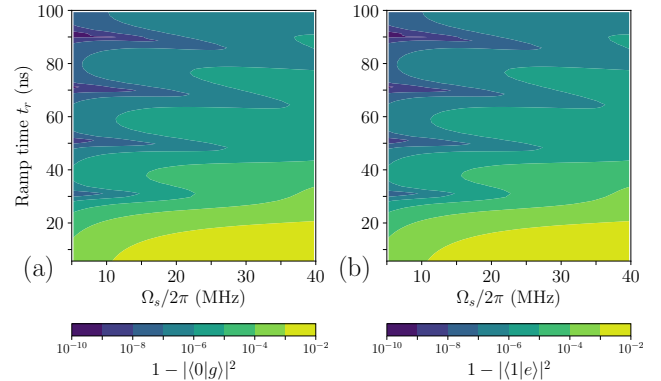


FIG. 4: Error for Q_1 in the adiabatical map from the dressed-qubit state $|0(1)\rangle$ to the bare state $|g(e)\rangle$ as a function of the ramp time t_r and the stark drive amplitude Ω_s . (a) Map from the dressed state $|0\rangle$ to the bare state $|g\rangle$. (b) Map from the dressed state $|1\rangle$ to the bare state $|e\rangle$. Here, the drive detuning is $\Delta_s/2\pi = 50$ MHz and pulse shape for the ramping process is $\Omega(t) = \Omega_s(1 - \cos[\pi(t - t_r)/t_r])/2$. Other system parameters are the same as those in Fig. 2.

mapping the dressed state to the corresponding bare state, and then the traditional readout can be employed. Therefore, the fidelities of the dressed-qubit initialization and readout depend on the applied ramp process. Figure 4 shows the fidelity of the adiabatical map from the dressed-qubit state $|0(1)\rangle$ to the bare state $|g(e)\rangle$ versus the ramp time t_r and the stark drive amplitude for Q_1 with the stark detuning $\Delta_s/2\pi = 50$ MHz. The pulse shape for ramp down process is $\Omega(t) = \Omega_s(1 - \cos[\pi(t - t_r)/t_r])/2$, where t_r denote the ramp time. As shown in Fig. 4, high-fidelity (99.9%) state maps can be realized within 30 ns.

However, note that for readout, especially for the dressed state $|1\rangle$, after mapping back to bare state $|e\rangle$ and without the protection of the stark drive, the readout fidelity may be limited by the lifetime of state $|e\rangle$. To address this, one may take the excited state promotion scheme, i.e., applying an additional π -pulse between the states $|1\rangle$ and $|2\rangle$ before the adiabatic map and the measurement, as demonstrated in previous works [58–60]. This scheme may effectively extend the lifetime of the bare state $|e\rangle$, thus improving the readout fidelity.

B. Gate operations

In this subsection, we examine the implementation of single-qubit X gates and two-qubit CZ gates on the proposed two-qubit system, in which a stark drive is applied to one of the two qubits. Note that in the following discussion, in the two-qubit system, single-qubit gates for one qubit are tuned up and characterized with the other qubit in its ground state.

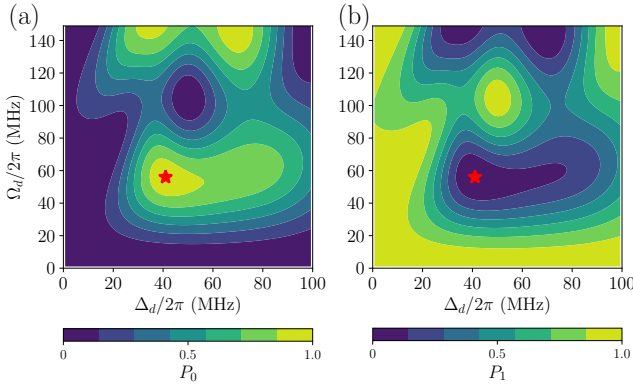


FIG. 5: Power Rabi oscillations for the microwave-dressed qubit. Population (a) P_0 and (b) P_1 (P_i denotes the population in the dressed state $|i\rangle$ at the end of the gate operation with fixed gate length $t_g = 20$ ns) as a function of the driving amplitude Ω_d and the driving detuning Δ_d of the pulse drive from the stark drive frequency. The red (light gray) star indicates the optimal parameter set for realizing a single-qubit X gate. Here, Q_1 is initialized in the dressed state $|1\rangle$. Other system parameters are the same as in Fig. 2. Note here that due to the weak anharmonicity of transmon qubits, during the gate operations, residual populations in the non-computational states, such as the second excited state, can exist. Thus, the sum of populations in computational states $|0\rangle$ and $|1\rangle$ is less than 1. With the help of the DRAG scheme [61], here, the population leakage is suppressed below 2×10^{-5} over the entire region.

1. Single-qubit gate operation

Here, we consider the implementation of single-qubit X gates. During the single-qubit gate operations, the bus frequency is biased at 5.7 GHz, giving rise to a residual ZZ coupling below 15 kHz. For both the microwave-dressed qubit and the bare qubit, single-qubit X gates are realized using the derivative removal by adiabatic gate (DRAG) scheme [61]. The pulse shape is $\Omega(t) = \Omega_x(t) + i\Omega_y(t)$ with

$$\Omega_x(t) = \frac{\Omega_d}{2}[1 - \cos(2\pi t/t_g)], \Omega_y(t) = -\frac{\alpha}{\eta}\dot{\Omega}_x(t), \quad (5)$$

where Ω_d is the peak pulse amplitude, t_g is the gate time, α is a free parameter for mitigating the leakage to nonoccupational energy levels. Similar to Ref.[43], the X gate is tuned up by adjusting the driving amplitude Ω_d and the detuning Δ_d of the pulse drive from the stark drive frequency for a fixed gate length ($t_g = 20$ ns) and $\alpha = 0.5$. Here, note that the optimal parameters for realizing X/2-gates can be found similarly by performing the power Rabi characterization with two consecutive pulses, and the single-qubit rotations around the Y-axis can be realized by controlling the phase of gate pulses, as indicated by Eq. (A7).

As high-fidelity single-qubit gates on the bare qubit have been well-demonstrated [1], here, we especially focus on the implementation of single-qubit gates for the microwave-dressed qubit. Firstly, we show that by applying an additional pulse drive to the dressed-qubit, Rabi oscillations between the

dressed qubit states can be realized, thus offering a way to realizing single-qubit gates. Considering that a stark drive with the drive detuning $\Delta_s/2\pi = 50$ MHz and the amplitude $\Omega_s/2\pi = 30$ MHz is applied to Q_1 , Figures 5 shows the power rabi oscillation versus the driving detuning Δ_d for the dressed qubit Q_1 initialized in the dressed state $|1\rangle$. The red (light gray) star in Fig. 5(a) indicates an optimal parameter sets for performing an almost perfect Rabi oscillation between $|0\rangle$ and $|1\rangle$.

Note that for microwave-dressed qubits, although Rabi oscillations can indeed be induced by adding an additional drive, as shown in Fig. 5, the dynamics seem more complex than that for undriven bare qubits (see Appendix A for details). This can be partially manifested by frequency difference between the optimal frequency of the pulse drive and the frequency of the microwave-dressed qubit. As marked by the red stars in Fig. 5, the detuning Δ_d of the optimal pulse drive frequency from the stark drive is about 40 MHz. However, according to the ac-stark shift in Fig. 3(a), the detuning of the microwave-dressed qubit Q_1 from the stark drive frequency should be about 60 MHz (recalling that $\Delta_s/2\pi = 50$ MHz, and the ac-stark shift is about $\delta\omega/2\pi = 10$ MHz for $\Omega_s/2\pi = 30$ MHz).

After finding the optimal parameter sets for implementing X gates, we can characterize the gate performance using the metric of gate fidelity [62]. Here, to quantify the performance of the (isolated) single-qubit X gate applied to one qubit (i.e., target qubit) in the coupled qubit system, we always assume that the other nearby qubit (i.e., spectator qubit) is in the ground state. Figure 6 shows the gate performance of the implemented single-qubit gates. In addition, the gate fidelity for simultaneously implementing single-qubit X gates is also presented. From these results, one can conclude that in the presence of a stark drive applied to one of the two coupled qubits, X gates applied to the bare qubit show worse gate performances (gate error $\sim 10^{-4}$) than that for the microwave-dressed qubits (gate error $\sim 10^{-5}$). Meanwhile, the performances for the simultaneous X gate operations are limited by the error from the bare qubits. After examining the system dynamics during the gate operations, these counterintuitive results can be explained by the interplay between the stark drive and the cross-driving crosstalk due to the qubit-qubit coupling [43], i.e., drives, such as the stark drive or the gate drive, applied to Q_1 can be felted by Q_2 and vice versa.

To further explore the exact nature of the extra error for bare qubits, in Fig. 7, we show the gate performance as a function of the frequency of Q_1 with Q_2 fixed at 5.2 GHz. Combined with inspections of the dynamics, we conclude that the presence of the peaked gate error can be attributed to various parasitic resonance transitions, resulting from the interplay between the stark drive and the cross-driving crosstalk. For example, in Fig. 7(a), where the stark drive is applied to Q_1 , the significant gate error at $\omega_1/2\pi = 5.0$ GHz is caused by the three-photon transition $|000\rangle \leftrightarrow |102\rangle$ and the two-photon transition $|001\rangle \leftrightarrow |102\rangle$. In Fig. 7(b), where the stark drive is applied to Q_2 , the significant gate error at $\omega_1/2\pi = 4.975$ GHz results from the two-photon transition $|000\rangle \leftrightarrow |002\rangle$ ($|100\rangle \leftrightarrow |102\rangle$), and single-photon transition $|000\rangle \leftrightarrow |001\rangle$ ($|100\rangle \leftrightarrow |101\rangle$) for $\omega_1/2\pi = 5.0375$ GHz.

Moreover, one can find that both the target qubit and the spectator qubit are involved in the parasitic transitions. Since under our definition of gate characterization, we assume that the spectator qubit is always in its ground state, thereby, these parasitic transitions can contribute to the isolated single-qubit errors, e.g., causing leakage error.

Additionally, we note that for the target qubit Q_2 , the peaked gate error at $\omega_1/2\pi = 4.95$ GHz, as shown in Fig. 7(a), are caused by the transitions $|000\rangle \leftrightarrow |002\rangle$ and $|001\rangle \leftrightarrow |002\rangle$. The two transitions are solely the result of the cross-driving from Q_1 , which is driven by a stark tone with a frequency of 4.90 GHz. For Q_2 , in principle, this cross-drive could be treated as an unintended stark drive. However, since the frequency of this unintended drive is on-resonance with the transitions involving high-energy levels, i.e., $|1\rangle \leftrightarrow |2\rangle$ of Q_2 , the descriptions that are based on two-level approximation, such as in Appendix A, break down, and the high-energy level $|2\rangle$ will affect the system dynamics significantly. In this situation, we argue that this unintended cross-drive will give rise to very nontrivial single-qubit addressing, causing the extra error at $\omega_1/2\pi = 4.95$ GHz for Q_2 .

Overall, the above analysis suggests that although the presence of the stark drive has only almost negligible effects on the gate performance for the microwave-dressed qubit, its effect on the gate performance for the nearby coupled bare qubit, which is coupled to the dressed qubit via a tunable bus, should be seriously considered. Recalling that during the single-qubit gate operations, the residual ZZ couplings are suppressed below 15 kHz. The above results further stress that:

(i) Besides residual ZZ coupling, cross-driving crosstalk due to qubit-qubit transversal coupling should also be taken into consideration for implementing high-fidelity gate operations [43]. Here, the presence of the stark drive and the cross-driving crosstalk together lead to parasitic transitions during single-qubit gate operations on bare qubits.

(ii) The suppression of ZZ coupling does not always mean that the transversal coupling between qubits, which can induce the cross-driving crosstalk, is also suppressed [63]. Besides ensuring the suppression of the ZZ coupling, these cross-driving induced parasitic transitions should also be minimized. The results shown in Fig. 7(b) suggest that for a given qubit-qubit detuning, choosing a suitable stark frequency can avoid these parasitic resonance transitions. In this way, the stark drive induced gate error is promising to be pushed below 10^{-4} .

2. Two-qubit CZ gate operation

To implement two-qubit CZ gates on the two-qubit system, where a stark drive is applied to one of the two qubits, we consider using the fast adiabatic scheme [43, 55]. During the gate operations, the tunable bus varies from the idle point at 5.7 GHz to the interaction point and then comes back according to the fast adiabatic pulse (see Appendix B for details). To implement fast CZ gates, e.g., sub-100-ns CZ gates, the interaction point should be near the resonance point for the interaction $|101\rangle \leftrightarrow |020\rangle$, where a large ZZ coupling with

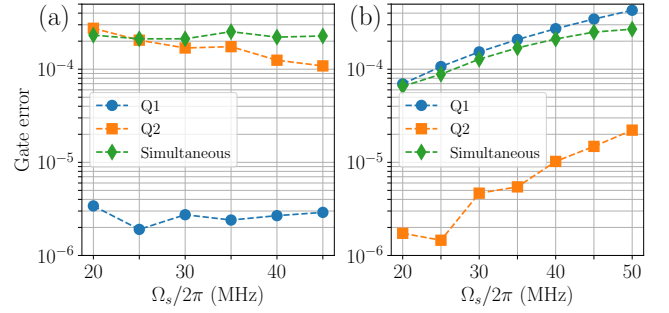


FIG. 6: Gate errors of the single-qubit X operations versus the stark drive amplitudes Ω_s . (a) The stark drive is applied to Q_1 with the drive detuning $\Delta_s/2\pi = 50$ MHz. (b) The stark drive is applied to Q_2 with the drive detuning $\Delta_s/2\pi = 70$ MHz. Other system parameters are the same as in Fig. 2.

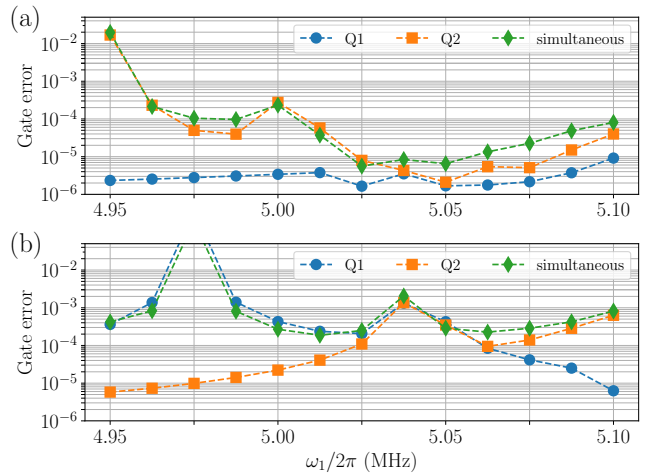


FIG. 7: Gate errors of the single-qubit X operations versus the frequency of Q_1 with Q_2 fixed at 5.2 GHz. (a) The stark drive is applied to Q_1 with the drive detuning $\Delta_s/2\pi = 50$ MHz and the drive amplitude $\Omega_s/2\pi = 20$ MHz. (b) The stark drive is applied to Q_2 with the drive detuning $\Delta_s/2\pi = 70$ MHz and the drive amplitude $\Omega_s/2\pi = 50$ MHz. Other system parameters are the same as in Fig. 2.

the strength of 10 MHz exists, as shown in Fig. 2. Similar to Ref.[43], the fidelity of the implemented CZ gates are then obtained by optimizing the pulse shape. Figure 8 shows the CZ gate error for various gate times and different stark drive amplitudes.

In Fig. 8(a), the stark drive is applied to Q_1 , and its detuning Δ_s is 50 MHz. One can find that CZ gate errors below 10^{-4} can be achieved with the gate time below 100 ns. More strikingly, in general, the larger the stark drive amplitude Ω_s , the worse the CZ gate fidelity becomes. In addition, one can also find that for gate time greater than certain values, gate error rises. Similar conclusions can also be obtained for the case where the stark drive is applied to Q_2 , as shown in Fig. 8(b).

As the discussion given in Fig. 2, these features can be explained by the presence of the parasitic resonance interactions with tiny energy gaps. These parasitic resonance interactions are caused by the stark drive, and involve both the qubits and the bus. During the gate operations, the qubit system will pass through or stay nearby to these parasitic resonance points. Generally, for leakage error due to the parasitic interactions with tiny strengths, the longer the gate time, the larger the error becomes [43]. The opposite is the case for leakage error resulting from the desired interaction $|101\rangle \leftrightarrow |020\rangle$. This trade-off results in the increased error shown in Fig. 8 for gate time exceeding certain values.

To show explicitly the presence of the parasitic resonance interactions, Figure 9 shows the ZZ coupling strength versus the bus frequency with different qubit detunings. Here, the Q_2 is fixed at 5.2 GHz. As shown in Figs. 9(a-c), for a given qubit-qubit detuning, when the amplitude of the stark drive applied to Q_1 decreases, dips and peaks caused by the parasitic interactions also slowly disappear, in line with the expectation (see also in Fig. 2). Similar results can also be obtained for the case where the stark drive applied to Q_2 , as shown in Figs. 9(d-e). Moreover, compared with the case where the stark drive applied to Q_1 , there exist more dips and peaks for the case where the stark drive applied to Q_2 . This explains that the gate performance is worse when the stark drive is applied to Q_2 , as shown in Fig. 8(b). This suggests that due to these parasitic interactions, even without the consideration of the qubit decoherence, long-time gates do not promise a better gate performance.

In addition, from the results shown in Fig. 9, we can conclude that the qubit-qubit detuning should be designed carefully to suppress the detrimental effect from the parasitic interactions in the tunable-bus architecture. As shown in Fig. 9(d-f), the smaller the qubit-qubit detuning, the more the parasitic interactions exist. Overall, the result shown in Fig. 8 and 9 suggests that besides the stark drive frequency and amplitude, the qubit-qubit detuning can also act as a control knob for avoiding the parasitic interactions. In this way, even with the presence of the stark drive for inducing the qubit frequency shift up to 20 MHz, sub-100-ns CZ gates can still be realized in the tunable-bus architecture with gate errors approaching 10^{-4} .

IV. FEASIBILITY

As demonstrated in previous works [18, 21], for the state-of-the-art transmon qubits, the TLS defects that are coupled strongly to qubits are generally sparse in spectrum. We thus expect that tuning qubit frequency by few MHz to tens of MHz can mitigate the loss due to the dominant TLS defect, thus stabilizing the qubit relaxation time. For fixed-frequency transmon qubits, this can be realized by using the off-resonance stark drive induced frequency shift. According to the discussion given in Sec. III, we show that although presence of stark drives can indeed cause additional gate errors in the tunable-bus architecture utilizing fixed-frequency transmon qubits, high-fidelity gate operations can still be achieved

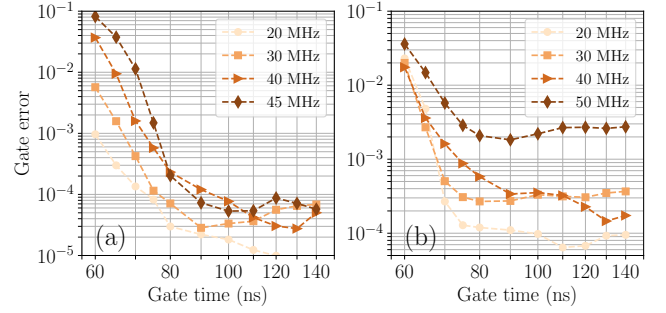


FIG. 8: Two-qubit CZ gate error versus the gate time with different stark drive amplitudes. (a) The stark drive is applied to Q_1 with the drive detuning $\Delta_s/2\pi = 50$ MHz, and the drive amplitude are (20, 30, 40, 45) MHz. (b) The stark drive is applied to Q_2 with the drive detuning $\Delta_s/2\pi = 70$ MHz, and the drive amplitude are (20, 30, 40, 50) MHz. Other system parameters are the same as in Fig. 2.

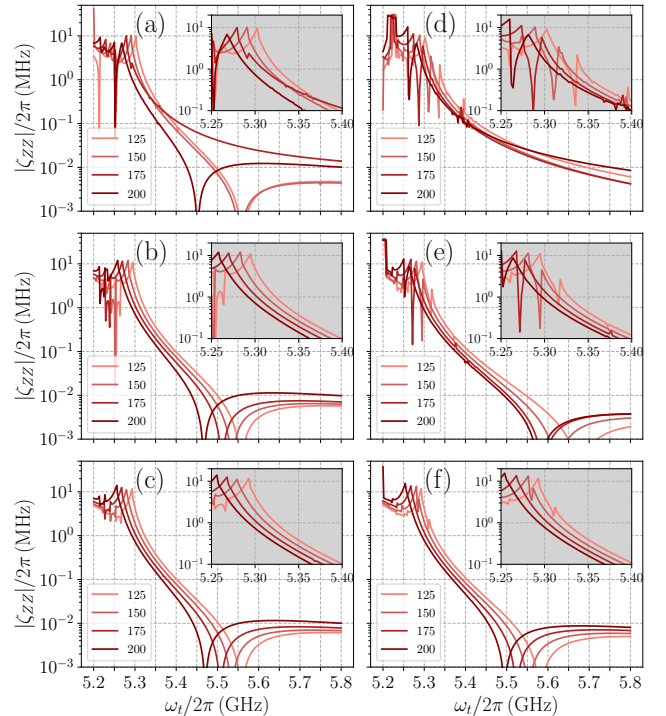


FIG. 9: ZZ coupling strength ζ_{ZZ} as a function of the bus frequency (ω_t) with different qubit-qubit detuning (125, 150, 175, 200) MHz. Here, Q_2 is fixed at 5.2 GHz. (a-c) The stark drive is applied to Q_1 with the drive detuning $\Delta_s/2\pi = 50$ MHz, and (d-f) for Q_2 with $\Delta_s/2\pi = 70$ MHz. The amplitude Ω_s of the stark drive are $|\Delta_s|$ in (a,d), $|\Delta_s|/2$ in (b,e), and $|\Delta_s|/4$ in (c,f). The insets enlarge the curves nearby the resonance points of the interaction $|101\rangle \leftrightarrow |020\rangle$. Other system parameters are the same as in Fig. 2.

by carefully choosing stark drive frequency, drive amplitude, and qubit-qubit detuning. As shown in Figs. 3, 6, and 8, we illustrate that one can effectively tune the qubit frequency up to 20 MHz through the ac-Stark shift, while implementing universal gates with errors below 0.001 on the tunable-bus architecture. By optimizing the stark drive frequency and amplitude, even lower gate error, e.g., below 0.0001, should be achieved. We thus expect that for fixed-frequency transmon qubits, the ac-stark shift should be a feasible tool for mitigating TLS-induced performance fluctuations while keeping the minimal impact on qubit control.

Note that the present study restricts to the case where the stark drive is only applied to one of the two qubits. Although the present analysis can also be applied to the case where both two qubits are subjected to the stark drives. We expect that in that case, the stark drive induced parasitic couplings will further limit the available parameter regions for implementing high-fidelity gate operations. Furthermore, for the state-of-art transmon qubit device, the TLS defects coupled strongly to qubits are generally both few in numbers and sparse in the spectrum [18, 21]. Thus, one can reasonably expect that the circumstance, where two coupled fixed-frequency transmon qubits are both coupled strongly to TLS defects at the same time, should be very rare.

V. CONCLUSION

In this work, we explore the possibility of combating TLS-induced temporal fluctuations in relaxation rates of fixed-frequency qubits with microwave-dressed states. Our analysis focus on the tunable-bus architecture, where fixed-frequency qubits are coupled via a tunable bus, however, we expect that many of our conclusions may also be applied to other qubit architectures utilizing fixed-frequency transmon qubits. While during gate operations, the stark drive can lead to additional gate errors due to parasitic interactions induced by the stark drive, one can mitigate their detrimental impacts on qubit control by carefully choosing the drive parameters and the system parameters. In this way, we show that one can effectively tune the qubit frequency through ac-Stark shift up to 20 MHz while keeping minimal impacts on the qubit control including qubit initialization, qubit readout, and gate operations.

Acknowledgments

We acknowledge helpful discussions with Yanwu Gu and Xinsheng Tan. This work was supported by the Beijing Natural Science Foundation (Grant No.Z190012), the National Natural Science Foundation of China (Grants No.11890704, No.12004042), and the Key-Area Research and Development Program of Guang Dong Province (Grant No. 2018B030326001). T.M. was supported by the National Natural Science Foundation of China (Grant No.11905100).

Appendix A: single-qubit gate operations with microwave-dressed qubits

For illustration purpose and without loss of generality, here we begin our analysis based on a two-level system subjected to two microwave drives, for which its dynamics is governed by the following Hamiltonian

$$H_{\text{lab}} = \frac{\omega_q}{2} \sigma_z + \Omega_s \cos(\omega_s t) \sigma_x + \Omega_d \cos(\omega_d t + \phi) \sigma_x, \quad (\text{A1})$$

where ω_q denotes the bare qubit transition frequency, Ω_s is the frequency of the stark drive (for effectively tuning the qubit frequency) with amplitude Ω_s , and ω_d is the frequency of the gate pulse drive (for implementing single-qubit gate operations) with amplitude Ω_d . ϕ denotes the relative phase between the stark drive and the gate pulse drive.

After applying the RWA, and moving into the rotating frame with respect to the off-resonant stark drive, the Hamiltonian can be expressed as $H_R = H_0 + H_I$ with

$$\begin{aligned} H_0 &= \frac{\Delta_s}{2} \sigma_z + \frac{\Omega_s}{2} \sigma_x, \\ H_I &= \frac{\Omega_d}{2} [\sigma^+ e^{-i(\Delta_d t + \phi)} + \sigma^- e^{+i(\Delta_d t + \phi)}], \end{aligned} \quad (\text{A2})$$

where $\Delta_s = \omega_q - \omega_s$ ($\Delta_d = \omega_d - \omega_s$) denotes the detuning of the qubit bare frequency (pulse driving frequency) from the stark driving frequency. Considering the unitary transformation $U_1 = \exp(-i\theta\sigma_y/2)$ with $\theta = \arctan(\Omega_s/\Delta_s)$ that intends to diagonalizing H_0 in the dressed qubit basis, (i.e., the dressed basis is defined as the eigenstates of H_0)

$$\begin{aligned} \{|1\rangle \equiv \sin \frac{\theta}{2} |g\rangle + \cos \frac{\theta}{2} |e\rangle, \\ |0\rangle \equiv \cos \frac{\theta}{2} |g\rangle - \sin \frac{\theta}{2} |e\rangle\}, \end{aligned} \quad (\text{A3})$$

one can obtain the following dressed system Hamiltonian $H_{\text{dress}} = U_1^\dagger H_R U_1$, (i.e., the Hamiltonian in the dressed basis)

$$\begin{aligned} H_{\text{dress}} &= [\Delta - \Omega_d \sin \theta \cos(\Delta_d t + \phi)] \frac{Z}{2} \\ &+ \Omega_d \cos \theta \cos(\Delta_d t + \phi) \frac{X}{2} \\ &+ \Omega_d \sin(\Delta_d t + \phi) \frac{Y}{2}, \end{aligned} \quad (\text{A4})$$

where $\Delta = \sqrt{\Delta_s^2 + \Omega_s^2}$ denotes the microwave-dressed qubit detuning, and $\{X = \cos \theta \sigma_x - \sin \theta \sigma_z, Y = \sigma_y, Z = \cos \theta \sigma_z + \sin \theta \sigma_x\}$ represent the Pauli operators defined on the dressed basis. According to the following unitary transformation [35, 64, 65]

$$U_2 = \exp \left(-i \frac{Z}{2} \left[\Delta t - \frac{\Omega_d \sin \theta}{\Delta_d} \sin(\Delta_d t + \phi) \right] \right), \quad (\text{A5})$$

and using the Jacobi-Anger relations, one can obtain the effective Hamiltonian $H_J = U_2^\dagger H_{\text{dress}} U_2 + i\partial_t(U_2^\dagger)U_2$, i.e.,

$$\begin{aligned}
H_J = & \frac{\Omega_d \cos \theta}{4} (e^{i\Delta_d t + i\phi} + e^{-i\Delta_d t - i\phi}) \\
& \times \left[e^{i\Delta_d t} S^+ \sum_{n=-\infty}^{\infty} J_n \left(\frac{\Omega_d \sin \theta}{\Delta_d} \right) e^{-in(\Delta_d t + \phi)} + h.c. \right] \\
& - \frac{\Omega_d}{4} (e^{i\Delta_d t + i\phi} - e^{-i\Delta_d t - i\phi}) \\
& \times \left[e^{i\Delta_d t} S^+ \sum_{n=-\infty}^{\infty} J_n \left(\frac{\Omega_d \sin \theta}{\Delta_d} \right) e^{-in(\Delta_d t + \phi)} - h.c. \right], \tag{A6}
\end{aligned}$$

where *h.c.* denotes the Hermitian conjugate, J_n is the n th order Bessel function of the first kind, and $S^\pm = (X \pm iY)/2$. Applying the RWA and dropping high-order Bessel functions, one can obtain the following effective Hamiltonian describing the usual single-qubit driven terms,

$$H_{\text{eff}} = \frac{\Omega_d \cos^2 \frac{\theta}{2}}{2} J_0 \left(\frac{\Omega_d \sin \theta}{\Delta_d} \right) \left[e^{-i\phi} S^+ e^{i(\Delta - \Delta_d)} + h.c. \right]. \tag{A7}$$

For system parameters used in the present work, one has $|\Delta_d| \sim |\Delta_s| \sim |\Delta|$ and the peak amplitude of the pulse drive $\Omega_d \sim |\Delta|$. We thus expect that the RWA breaks and other terms given in Eq. A6, which involve high-order Bessel functions, can have non-negligible effects on the system dynamics. When considering $\Delta_d \approx \Delta$, these terms contribute as off-resonance transitions during the single-gate operations, thus shifting the frequency of the dressed qubit [35, 65, 66]. This

can explain the frequency mismatch discussed in Sec. III B 1.

Appendix B: Pulse shaping for implementing two-qubit CZ gates

In the present work, similar to Ref.[43], we use the fast adiabatic gate scheme for implementing CZ gates by tuning the bus frequency. Here, for easy reference, we give brief descriptions of the pulse shape for realizing CZ gates. During the CZ gate operation, the tunable bus frequency ω_t varies from the idle point (θ_i) to the interaction point (θ_f) and then back according to a fast adiabatic pulse. Expressed in terms of Fourier basis functions, the pulse shape is described as [55]

$$\theta(t) = \theta_i + \frac{\theta_f - \theta_i}{2} \sum_{n=1,2,3,\dots} \lambda_n \left[1 - \cos \frac{2n\pi t}{T} \right] \tag{B1}$$

with constraints on the odd coefficients $\sum_{n \text{ odd}} \lambda_n = 1$. Here, the control angle is defined as $\theta \equiv \arctan(2J_{101}/\Delta_{101})$, where J_{101} represents the strength of the interaction $|101\rangle \leftrightarrow |020\rangle$, Δ_{101} represents the detuning of the qubit system from the resonance point of the interaction $|101\rangle \leftrightarrow |020\rangle$, and T is the gate time.

For implementing CZ gates, we consider the pulse shape defined in Eq. B1 with three Fourier terms, for which the associated coefficients are $\{\lambda_1, \lambda_2, 1 - \lambda_1\}$. The free parameters $\{\lambda_1, \lambda_2, \theta_f\}$ are then determined by numerically optimizing the CZ gate fidelity.

[1] M. Kjaergaard, M. E. Schwartz, J. Braumüller, P. Krantz, J. I.-Jan Wang, S. Gustavsson, and W. D. Oliver, Superconducting qubits: Current state of play, *Annu. Rev. Condens. Matter Phys.* **11**, 369 (2020).

[2] A. P. M. Place, L. V. H. Rodgers, P. Mundada, B. M. Smitham, M. Fitzpatrick, Z. Leng, A. Premkumar, J. Bryon, A. Vrajitoarea, S. Sussman *et al.*, New material platform for superconducting transmon qubits with coherence times exceeding 0.3 milliseconds, *Nat. Commun.* **12**, 1779 (2021).

[3] C. Wang, X. Li, H. Xu, Z. Li, J. Wang, Z. Yang, Z. Mi, X. Liang, T. Su, C. Yang *et al.*, Towards practical quantum computers: transmon qubit with a lifetime approaching 0.5 milliseconds, *npj Quantum Inf.* **8**, 3 (2022).

[4] R. T. Gordon, C. E. Murray, C. Kurter, M. Sandberg, S. A. Hall, K. Balakrishnan, R. Shelby, B. Wacaser, A. A. Stabile, J. W. Sleight *et al.*, Environmental Radiation Impact on Lifetimes and Quasiparticle Tunneling Rates of Fixed-Frequency Transmon Qubits, *Appl. Phys. Lett.* **120**, 074002 (2022).

[5] J. Koch, T. M. Yu, J. Gambetta, A. A. Houck, D. I. Schuster, J. Majer, A. Blais, M. H. Devoret, S. M. Girvin, and R. J. Schoelkopf, Charge-insensitive qubit design derived from the cooper pair box, *Phys. Rev. A* **76**, 042319 (2007).

[6] J. M. Chow, J. M. Gambetta, A. D. Córcoles, S. T. Merkel, J. A. Smolin, C. Rigetti, S. Poletto, G. A. Keefe, M. B. Rothwell, J. R. Rozen, M. B. Ketchen, and M. Steffen, Universal Quantum Gate Set Approaching Fault-Tolerant Thresholds with Superconducting Qubits, *Phys. Rev. Lett.* **109**, 060501 (2012).

[7] S. Poletto, J. M. Gambetta, S. T. Merkel, J. A. Smolin, J. M. Chow, A. D. Córcoles, G. A. Keefe, M. B. Rothwell, J. R. Rozen, D. W. Abraham, C. Rigetti, and M. Steffen, Entanglement of two superconducting qubits in a waveguide cavity via monochromatic two-photon excitation, *Phys. Rev. Lett.* **109**, 240505 (2012).

[8] J. M. Chow, J. M. Gambetta, A. W. Cross, S. T. Merkel, C. Rigetti, and M. Steffen, Microwave-activated conditional-phase gate for superconducting qubits, *New J. Phys.* **15**, 115012 (2013).

[9] H. Paik, A. Mezzacapo, Ma. Sandberg, D. T. McClure, B. Abdo, A. D. Córcoles, O. Dial, D. F. Bogorin, B. L. T. Plourde, M. Steffen, A. W. Cross, J. M. Gambetta, and J. M. Chow, Experimental Demonstration of a Resonator-Induced Phase Gate in a Multiqubit Circuit-QED System, *Phys. Rev. Lett.* **117**, 250502 (2016).

[10] S. P. Premaratne, J.-H. Yeh, F. C. Wellstood, and B. S. Palmer, Implementation of a generalized controlled-NOT gate between fixed-frequency transmons, *Phys. Rev. A* **99**, 012317 (2019).

[11] S. Krinner, P. Kurpiers, B. Royer, P. Magnard, I. Tsitsilin, J.-C. Besse, A. Remm, A. Blais, and A. Wallraff, Demonstration of an All-Microwave Controlled-Phase Gate between Far-Detuned Qubits, *Phys. Rev. Appl.* **14**, 044039 (2020).

[12] B. K. Mitchell, R. K. Naik, A. Morvan, A. Hashim, J. M. Kreikebaum, B. Marinelli, W. Lavrijsen, K. Nowrouzi, D.

I. Santiago, and I. Siddiqi, Hardware-Efficient Microwave-Activated Tunable Coupling between Superconducting Qubits, *Phys. Rev. Lett.* **127**, 200502 (2021).

[13] K. X. Wei, E. Magesan, I. Lauer, S. Srinivasan, D. F. Bogorin, S. Carnevale, G. A. Keefe, Y. Kim, D. Klaus, W. Landers *et al.*, Quantum crosstalk cancellation for fast entangling gates and improved multi-qubit performance, [arXiv:2106.00675](https://arxiv.org/abs/2106.00675).

[14] D. C. McKay, S. Filipp, A. Mezzacapo, E. Magesan, J. M. Chow, and J. M. Gambetta, Universal gate for fixed-frequency qubits via a tunable bus, *Phys. Rev. Appl.* **6**, 064007 (2016).

[15] M. C. Collodo, J. Herrmann, N. Lacroix, C. K. Andersen, A. Remm, S. Lazar, J. Besse, T. Walter, A. Wallraff, and C. Eichler, Implementation of Conditional Phase Gates Based on Tunable ZZ Interactions, *Phys. Rev. Lett.* **125**, 240502 (2020).

[16] Y. Xu, J. Chu, J. Yuan, J. Qiu, Y. Zhou, L. Zhang, X. Tan, Y. Yu, S. Liu, J. Li, F. Yan, and D. Yu, High-Fidelity, High-Scalability Two-Qubit Gate Scheme for Superconducting Qubits, *Phys. Rev. Lett.* **125**, 240503 (2020).

[17] S. S. Hong, A. T. Papageorge, P. Sivarajah, G. Crossman, N. Didier, A. M. Polloreno, E. A. Sete, S. W. Turkowski, M. P. da Silva, and B. R. Johnson, Demonstration of a parametrically activated entangling gate protected from flux noise, *Phys. Rev. A* **101**, 012302 (2020).

[18] P.V. Klimov, J. Kelly, Z. Chen, M. Neeley, A. Megrant, B. Burkett, R. Barends, K. Arya, B. Chiaro, Y. Chen *et al.*, Fluctuations of Energy-Relaxation Times in Superconducting Qubits, *Phys. Rev. Lett.* **121**, 090502 (2018).

[19] J. J. Burnett, A. Bengtsson, M. Scigliuzzo, D. Niegce, M. Kudra, P. Delsing, and J. Bylander, Decoherence benchmarking of superconducting qubits, *npj Quantum Inf.* **5**, 54 (2019).

[20] S. Schlör, J. Lisenfeld, C. Müller, A. Bilmes, A. Schneider, D. P. Pappas, A. V. Ustinov, and M. Weides, Correlating Decoherence in Transmon Qubits: Low Frequency Noise by Single Fluctuators, *Phys. Rev. Lett.* **123**, 190502 (2019).

[21] M. Carroll, S. Rosenblatt, P. Jurcevic, I. Lauer, and A. Kandala, Dynamics of superconducting qubit relaxation times, [arXiv:2105.15201](https://arxiv.org/abs/2105.15201).

[22] Y. Kim, C. J. Wood, T. J. Yoder, S. T. Merkel, J. M. Gambetta, K. Temme, and A. Kandala, Scalable error mitigation for noisy quantum circuits produces competitive expectation values, [arXiv:2108.09197](https://arxiv.org/abs/2108.09197).

[23] J. Burnett, L. Faoro, I. Wisby, V. L. Gurtovoi, A. V. Chernykh, G. M. Mikhailov, V. A. Tulin, R. Shaikhaidarov, V. Antonov, P. J. Meeson, A. Ya. Tzalenchuk, and T. Lindström, Evidence for interacting two-level systems from the 1/f noise of a superconducting resonator, *Nat. Commun.* **5**, 4119 (2014).

[24] C. Müller, J. Lisenfeld, A. Shnirman, and S. Poletto, Interacting two-level defects as sources of fluctuating high-frequency noise in superconducting circuits, *Phys. Rev. B* **92**, 035442 (2015).

[25] L. Faoro and L. B. Ioffe, Interacting tunneling model for two-level systems in amorphous materials and its predictions for their dephasing and noise in superconducting microresonators, *Phys. Rev. B* **91**, 014201 (2015).

[26] J. H. Béjanin, C. T. Earnest, A. S. Sharafeldin, and M. Mariantoni, Interacting defects generate stochastic fluctuations in superconducting qubits, *Phys. Rev. B* **104**, 094106 (2021).

[27] U. Vool, I. M. Pop, K. Sliwa, B. Abdo, C. Wang, T. Brecht, Y. Y. Gao, S. Shankar, M. Hatridge, G. Catelani *et al.*, Non-Poissonian Quantum Jumps of a Fluxonium Qubit due to Quasiparticle Excitations, *Phys. Rev. Lett.* **113**, 247001 (2014).

[28] S. Gustavsson, F. Yan, G. Catelani, J. Bylander, A. Kamal, J. Birenbaum, D. Hover, D. Rosenberg, G. Samach, A. P. Sears *et al.*, Suppressing relaxation in superconducting qubits by quasiparticle pumping, *Science* **354**, 1573 (2016).

[29] F. Yan, S. Gustavsson, A. Kamal, J. Birenbaum, A. P. Sears, D. Hover, T. J. Gudmundsen, D. Rosenberg, G. Samach, S. Weber *et al.*, The flux qubit revisited to enhance coherence and reproducibility, *Nat. Commun.* **7**, 12964 (2016).

[30] K. Li, S. Dutta, R. Zhang, Z. Steffen, D. Poppert, J. Bowser, S. Keshvari, B. Palmer, C. J. Lobb and F. C. Wellstood, Large fluctuations of T_1 in long-lived transmon qubits, *Bulletin of the American Physical Society*, 2021.

[31] R. Zhang, Loss in Superconducting Quantum Devices from Non-equilibrium Quasiparticles and Inhomogeneity in Energy Gap. PhD thesis. University of Maryland, College Park, 2021.

[32] S. E. de Graaf, L. Faoro, L. B. Ioffe, S. Mahashabde, J. J. Burnett, T. Lindström, S. E. Kubatkin, A. V. Danilov, and A. Y. Tzalenchuk, Two-level systems in superconducting quantum devices due to trapped quasiparticles, *Sci. Adv.* **6**, eabc5055 (2020).

[33] J. Kelly, P. O’Malley, M. Neeley, H. Neven, and J. M. Martinis, Physical qubit calibration on a directed acyclic graph, [arXiv:1803.03226](https://arxiv.org/abs/1803.03226).

[34] C. Müller, J. H. Cole, and J. Lisenfeld, Towards understanding two-level-systems in amorphous solids: insights from quantum circuits, *Rep. Prog. Phys.* **82**, 124501 (2019).

[35] J. Tuorila, M. Silveri, M. Sillanpää, E. Thuneberg, Y. Makhlin, and P. Hakonen, Stark Effect and Generalized Bloch-Siegert Shift in a Strongly Driven Two-Level System, *Phys. Rev. Lett.* **105**, 257003 (2010).

[36] A. Schneider, J. Braumüller, L. Guo, P. Stehle, H. Rotzinger, M. Marthaler, A. V. Ustinov, and M. Weides, Local sensing with the multilevel ac stark effect, *Phys. Rev. A* **97**, 062334 (2018).

[37] G. Oelsner, U. Hübner, and E. Il’ichev, Controlling the energy gap of a tunable two-level system by ac drive, *Phys. Rev. B* **101**, 054511 (2020).

[38] C. Cohen-Tannoudji, J. Dupont-Roc, and G. Grynberg, *Atom-Photon Interactions* (Wiley, New York, 1998).

[39] C. Rigetti, A. Blais, and M. Devoret, Protocol for Universal Gates in Optimally Biased Superconducting Qubits, *Phys. Rev. Lett.* **94**, 240502 (2005).

[40] Y.-x. Liu, C. P. Sun, and F. Nori, Scalable superconducting qubit circuits using dressed states, *Phys. Rev. A* **74**, 052321 (2006).

[41] C. M. Wilson, T. Duty, F. Persson, M. Sandberg, G. Johansson, and P. Delsing, Coherence Times of Dressed States of a Superconducting Qubit under Extreme Driving, *Phys. Rev. Lett.* **98**, 257003 (2007).

[42] Q. Guo, S.-B. Zheng, J. Wang, C. Song, P. Zhang, K. Li, W. Liu, H. Deng, K. Huang, D. Zheng *et al.*, Dephasing-Insensitive Quantum Information Storage and Processing with Superconducting Qubits, *Phys. Rev. Lett.* **121**, 130501 (2018).

[43] P. Zhao, K. Linghu, Z. Li, P. Xu, R. Wang, G. Xue, Y. Jin, and H. Yu, Quantum crosstalk analysis for simultaneous gate operations on superconducting qubits, [arXiv:2110.12570](https://arxiv.org/abs/2110.12570).

[44] G. Ithier, E. Collin, P. Joyez, P. J. Meeson, D. Vion, D. Esteve, F. Chiarello, A. Shnirman, Y. Makhlin, J. Schriefl, and G. Schön, Decoherence in a superconducting quantum bit circuit, *Phys. Rev. B* **72**, 134519 (2005).

[45] J. Jing, P. Huang, and X. Hu, Decoherence of an electrically driven spin qubit, *Phys. Rev. A* **90**, 022118 (2014).

[46] T. J. Green, J. Sastrawan, H. Uys, and M. J. Biercuk, Arbitrary Quantum Control of Qubits in the Presence of Universal Noise, *New J. Phys.* **15**, 095004 (2013).

[47] H. Ball, W. D Oliver, and M. J Biercuk, The role of master clock stability in quantum information processing, *npj Quantum Inf.* **2**, 16033 (2016).

[48] J. P. G. van Dijk, E. Kawakami, R. N. Schouten, M. Veldhorst,

L. M. K. Vandersypen, M. Babaie, E. Charbon, and F. Sebas-
tiano, Impact of Classical Control Electronics on Qubit Fidelity,
Phys. Rev. Appl. **12**, 044054 (2019).

[49] M. Werninghaus, D. J. Egger, F. Roy, S. Machnes, F. K. Wil-
helm, and S. Filipp, Leakage reduction in fast superconducting
qubit gates via optimal control, *npj Quantum Inf.* **7**, 14 (2021).

[50] R. Barends, C. M. Quintana, A. G. Petukhov, Y. Chen, D. Kafri,
K. Kechedzhi *et al.*, Diabatic Gates for Frequency-Tunable Su-
perconducting Qubits, *Phys. Rev. Lett.* **123**, 210501 (2019).

[51] A. Noguchi, A. Osada, S. Masuda, S. Kono, K. Heya, S. P.
Wolski, H. Takahashi, T. Sugiyama, D. Lachance-Quirion, and
Y. Nakamura, Fast parametric two-qubit gates with suppressed
residual interaction using the second-order nonlinearity of a cu-
bic transmon, *Phys. Rev. A* **102**, 062408 (2020).

[52] X. Xu and M.H. Ansari, ZZ freedom in two qubit gates, *Phys.
Rev. Applied* **15**, 064074 (2021).

[53] H. Xiong, Q. Ficheux, A. Somoroff, L. B. Nguyen, E. Dogan,
D. Rosenstock, C. Wang, K. N. Nesterov, M. G. Vavilov, and V.
E. Manucharyan, Arbitrary controlled-phase gate on fluxonium
qubits using differential ac-Stark shifts, [arXiv:2103.04491](https://arxiv.org/abs/2103.04491).

[54] Z. Ni, S. Li, L. Zhang, J. Chu, J. Niu, T. Yan, X. Deng, L. Hu,
J. Li, Y. Zhong, S. Liu, F. Yan, Y. Xu, and Dapeng Yu, Scalable
method for eliminating residual ZZ interaction between super-
conducting qubits, [arXiv:2111.13292](https://arxiv.org/abs/2111.13292).

[55] J. M. Martinis and M. R. Geller, Fast adiabatic qubit gates using
only σ_z control, *Phys. Rev. A* **90**, 022307 (2014).

[56] A. E. Seedhouse, I. Hansen, A. Laucht, C. H. Yang, A. S. Dzu-
rak, and A. Saraiva, Quantum computation protocol for dressed
spins in a global field, *Phys. Rev. B* **104**, 235411 (2021).

[57] Z. Huang, P. S. Mundada, A. Gyenis, D. I. Schuster, A. A.
Houck, and J. Koch, Engineering Dynamical Sweet Spots to
Protect Qubits from $1/f$ Noise, *Phys. Rev. Appl.* **15**, 034065
(2021).

[58] F. Mallet, F. R. Ong, A. Palacios-Laloy, F. Nguyen, P. Bertet, D.
Vion, and D. Esteve, Single-shot qubit readout in circuit quan-
tum electrodynamics, *Nat. Phys.* **5**, 791 (2009).

[59] S. S. Elder, C. S. Wang, P. Reinhold, C. T. Hann, K. S. Chou,
B. J. Lester, S. Rosenblum, L. Frunzio, L. Jiang, and R. J.
Schoelkopf, High-Fidelity Measurement of Qubits Encoded in
Multilevel Superconducting Circuits, *Phys. Rev. X* **10**, 011001
(2020).

[60] P. Jurcevic, A. Javadi-Abhari, L. S. Bishop, I. Lauer, D. F. Bo-
gorin *et al.*, Demonstration of quantum volume 64 on a super-
conducting quantum computing system, *Quantum Sci. Technol.*
6, 025020 (2021).

[61] F. Motzoi, J. M. Gambetta, P. Rebentrost, and F. K. Wilhelm,
Simple Pulses for Elimination of Leakage in Weakly Nonlinear
Qubits, *Phys. Rev. Lett.* **103**, 110501 (2009).

[62] L. H. Pedersen, N. M. Møller, and K. Mølmer, Fidelity of quan-
tum operations, *Phys. Lett. A* **367**, 47 (2007).

[63] P. Zhao, D. Lan, P. Xu, G. Xue, M. Blank, X. Tan, H. Yu, and
Y. Yu, Suppression of Static ZZ Interaction in an All-Transmon
Quantum Processor, *Phys. Rev. Appl.* **16**, 024037 (2021).

[64] W. D. Oliver, Y. Yu, J. C. Lee, K. K. Berggren, L. S. Levitov,
and T. P. Orlando, Mach-Zehnder interferometry in a strongly
driven superconducting qubit, *Science* **310**, 1653 (2005).

[65] A. P. Saiko, G. G. Fedoruk, and S. A. Markevich, Effective field
and the Bloch-Siegert shift at bichromatic excitation of multi-
photon EPR, *JETP Lett.* **84**, 130 (2006).

[66] Y. Yan, Z. Lü, J. Luo, and H. Zheng, Effects of counter-rotating
couplings of the Rabi model with frequency modulation, *Phys.
Rev. A* **96**, 033802 (2017).